Chinese Chemical Letters 32 (2021) 3450–3456

Contents lists available at ScienceDirect

Chinese Chemical Letters

journal homepage: www.elsevier.com/locate/cclet

Communication

Bandgap engineering of tetragonal phase $CuFeS_2$ quantum dots *via* mixed-valence single-atomic Ag decoration for synergistic Cr(VI) reduction and RhB degradation

Yangzi Shangguan[a,b], Yuanhao Zhou[b], Renji Zheng[b], Xuezhen Feng[b], Qiuyue Ge[a,b], Ranhao Wang[b], Dazhong Yang[b], Wenfei Wei[b], Xiaoyong Wu[c], Jia Lin[a,*], Hong Chen[b,*]

[a] *Department of Physics, Shanghai Key Laboratory of Materials Protection and Advanced Materials in Electric Power, Shanghai University of Electric Power, Shanghai 200090, China*

[b] *State Environmental Protection Key Laboratory of Integrated Surface Water-Groundwater Pollution Control, Guangdong Provincial Key Laboratory of Soil and Groundwater Pollution Control, School of Environmental Science and Engineering, Southern University of Science and Technology, Shenzhen 518055, China*

[c] *Hubei Key Laboratory of Mineral Resources Processing and Environment, School of Resources and Environmental Engineering, Wuhan University of Technology, Wuhan 430070, China*

ARTICLE INFO

Article history:
Received 20 February 2021
Revised 30 March 2021
Accepted 19 May 2021
Available online 24 May 2021

Keywords:
Single-atom catalysts
Bandgap engineering
Cr(VI) reduction
Organic pollutants degradation
Dyeing wastewater treatment

ABSTRACT

Bandgap engineering through single-atom site binding on semiconducting photocatalyst can boost the intrinsic activity, selectivity, carrier separation, and electron transport. Here, we report a mixed-valence Ag(0) and Ag(I) single atoms co-decorated semiconducting chalcopyrite quantum dots ($Ag/CuFeS_2$ QDs) photocatalyst. It demonstrates efficient photocatalytic performances for specific organic dye (rhodamine B, denoted as RhB) as well as inorganic dye (Cr(VI)) removal in water under natural sunlight irradiation. The RhB degradation and Cr(VI) removal efficiencies by $Ag/CuFeS_2$ QDs were 3.55 and 6.75 times higher than those of the naked $CuFeS_2$ QDs at their optimal pH conditions, respectively. Besides, in a mixture of RhB and Cr(VI) solution under neutral condition, the removal ratio has been elevated from 30.2% to 79.4% for Cr(VI), and from 95.2% to 97.3% for RhB degradation by using $Ag/CuFeS_2$ QDs after 2 h sunlight illumination. The intrinsic mechanism for the photocatalytic performance improvement is attributed to the narrow bandgap of the single-atomic Ag(I) anchored $CuFeS_2$ QDs, which engineers the electronic structure as well as expands the optical light response range. Significantly, the highly active $Ag(0)/CuFeS_2$ and $Ag(I)/CuFeS_2$ effectively improve the separation efficiency of the carriers, thus enhancing the photocatalytic performances. This work presents a highly efficient single atom/QDs photocatalyst, constructed through bandgap engineering via mixed-valence single noble metal atoms binding on semiconducting QDs. It paves the way for developing high-efficiency single-atom photocatalysts for complex pollutions removal in dyeing wastewater environment.

Inorganic heavy metal ions and organic dye pollutants are severe pollution sources in dyeing wastewater, which causes many negative impacts on human health and natural environment [1]. Among all the different types of dyes, inorganic Cr(VI) and organic RhB given the various dye wastewater treatment technologies, photocatalysis has attracted broad attention due to its economic feasibility and high efficiency [2]. Among the different types of photocatalysts, single-atomic semiconductor-based photocatalyst has become one of the most promising photocatalytic materials due to its maximum atom utilization and excellent redox catalytic properties, which has been developed very fast in clear energy catalysis recently and need to be urgently explored for wastewater treatment [3]. To construct a high efficient single-atomic semiconducting photocatalyst, engineering the single-atomic metal homogeneously dispersed on a high efficient semiconductor is of crucial importance. Among all the reported semiconducting materials, $CuFeS_2$ quantum dots (QDs) are a kind of promising ultraviolet-visible-infrared (UV–vis-NIR) semiconductor photocatalytic material with a tunable bandgap, size-dependent quantum confinement effect, high surface area, as well as "mixed redox-couple of Cu(I)−S−Fe(III)" in its crystal structure [4]. It has been widely used

* Corresponding authors.
E-mail addresses: jlin@shiep.edu.cn (J. Lin), chenh3@sustech.edu.cn (H. Chen).

https://doi.org/10.1016/j.cclet.2021.05.040
1001-8417/

in the field of photodetection [5], fluorescence labeling [6,7], electrocatalysis [8,9], and photocatalysis [10,11]. It can be activated by photons with energy greater than the bandgap (E_g) to produce electron-hole pairs. These photogenerated electron-hole pairs can be further separated and migrated to the surface of the QDs and undergo a strong reduction/oxidation reaction with an electron acceptor/donor adsorbed on the catalyst surface [12]. At present, the photocatalytic performance of the photocatalysts is frequently limited by the fast recombination of the photogenerated electron-hole pairs. To overcome this disadvantage, various strategies have been developed, including the deposition of noble metal [13,14], construction of heterojunctions [15], as well as the sensitization of the semiconductor with adsorbed dye molecules [16]. Besides, introducing active single atoms to strengthen the metal-support interactions is a widely used strategy that can maximize the atomic efficiency, change the adsorption and desorption properties of the surface, optimize the intrinsic activity of catalysts, and reduce the cost of noble metal catalysts [17]. Single atoms deposited on support surface act as electron acceptor to provide highly efficient electron transfer channels, hence prevent the fast recombination of the photogenerated electron-hole pairs, greatly boost the photocatalytic activity [18]. The selectivity and catalytic activity of the catalyst can be modulated by monatomic modification to selectively remove harmful substances in wastewater. However, studies on the formation and catalytic mechanism of single-atomic photocatalysts for environmental pollutant treatment are still rare up to now [19].

In this work, mixed-valence single-atomic Ag(I) and Ag(0) co-decorated $CuFeS_2$ QDs ($Ag/CuFeS_2$ QDs) are reported firstly with a high Ag loading of 3.63 wt%. Based on the characterization results of aberration-corrected high-angle annular dark-field scanning transmission electron microscopy (HAADF-STEM), X-ray diffraction (XRD), and X-ray photoelectron spectroscopy (XPS), we confirm that mixed-valence single-atomic Ag is uniformly distributed on the surface of the $CuFeS_2$ QDs. Benefited from the formation of the mixed-valence single-atomic $Ag/CuFeS_2$, the bandgap of $CuFeS_2$ has been significantly lowered down to 1.21 eV. With the significant electron capture capability of metallic Ag single atoms, the charge carrier separation efficiency has been improved dramatically. The narrower bandgap of $Ag/CuFeS_2$ promotes the photocatalyst performance by extending its absorption light spectrum up to the near-infrared (NIR) light range. Further, combine the density functional theory (DFT) calculations, the formation and catalytic mechanisms of monatomic catalysts are illustrated, which suggests that the introduction of Ag atoms can facilitate the engineering of the $CuFeS_2$ QDs bandgap. Contributed from its small particle sizes and low surface states [20], this mixed-valence Ag(0) and Ag(I) single-atom co-decorated semiconducting photocatalyst exhibits a stronger reduction power with its photoexcited electrons, which can give impetus to the photocatalytic treatment of diverse environmental pollutions in complex environmental media such as dyeing wastewater.

High-purity dark purple $CuFeS_2$ QDs were prepared through a colloidal synthesis approach [4]. The $Ag/CuFeS_2$ catalyst was prepared *via* the photoreduction method at room temperature, as shown in Text S1 (Supporting information). The obtained $Ag/CuFeS_2$ catalysts showed a high metal loading of 3.63 wt% determined by inductive coupled plasma mass spectrometry (ICP-MS) (Table S1 in Supporting information). To investigate the crystal structure and electronic structure of $Ag/CuFeS_2$, a series of characterizations, including XRD, XPS, and ultraviolet-visible diffuse reflectance spectra (UV–vis DRS) have been employed. Fig. 1a depicted the XRD patterns of $CuFeS_2$ and $Ag/CuFeS_2$ QDs. The predominant diffraction peaks in both samples were located at 2θ values of 29.3°, 33.8°, 48.6° and 57.8°, which could be assigned to the diffraction peaks from (112), (200), (220) and (400) lattice planes of the tetragonal phase $CuFeS_2$ (JCPDS No. 37−0471). This observation indicated that $CuFeS_2$ was crystallized in the tetragonal crystal system with a space group of I–42d [21]. Moreover, no characteristic diffraction peaks of the metallic Ag were observed in $Ag/CuFeS_2$ QDs, which supported that the Ag atoms were uniformly dispersed on $CuFeS_2$ QDs support, and no particular-sized Ag was formed within $Ag/CuFeS_2$ QDs. XPS was further used to study the valence state of Ag. As shown in Fig. 1b, characteristic peaks of Ag have been observed, the two doublet 3d peaks in the high-resolution XPS spectrum of Ag 3d (Fig. 1c) indicated that there were two different chemical states for Ag species. The Ag $3d_{5/2}$ and Ag $3d_{3/2}$ peaks with binding energies of 367.7 and 373.7 eV could be ascribed to mono valence state of Ag(I); while the other doublet at 368.2 and 374.2 eV for Ag $3d_{5/2}$ and Ag $3d_{3/2}$, respectively, could be assigned to the metallic Ag(0) [22,23]. The relative content of metallic Ag(0) to Ag(I) was calculated to be 43.2%. These results suggested that Ag single atoms were located on QD surfaces as a mixed-valence state. Beyond that, the Cu 2p level in $Ag/CuFeS_2$ QDs has been split into $2p_{3/2}$ and $2p_{1/2}$ peaks at 932.0 and 951.8 eV; while Fe $2p_{3/2}$ was characterized with binding energies of 711.6 eV; the Fe $2p_{1/2}$ peak was with binding energies of 723.9 eV. These observations suggested that the valence state of Cu in $Ag/CuFeS_2$ remained as +1 state [24], and the Fe could be described with *a* +3 valence state (Figs. S1a and b in Supporting information) [25]. No variation in the valence states of Cu and Fe indicated that there was no redox reaction occurred after single-atomic Ag decorating on $CuFeS_2$ QDs.

In terms of photocatalysis performance, bandgap engineering and charge-carriers have a significant influence on the performance of the semiconducting photocatalyst. As shown in Fig. 1d, the pure tetragonal phase $CuFeS_2$ QDs exhibited a bandgap of 1.34 eV, when single Ag atoms were introduced, the bandgap of the material decreased to 1.21 eV. Furthermore, Mott-Schottky (MS) measurements, as shown in Fig. 1e indicated that the $CuFeS_2$ and $Ag/CuFeS_2$ QDs were both n-type semiconductors. It could conclude that the experimental flat-band potential of $Ag/CuFeS_2$ was −0.07 V (*vs.* NHE). Furthermore, it was generally known that the bottom of the conduction bands in many n-type semiconductors was more negative by about −0.2 V than the flat-band potential, which indicated that the conduction band bottom of $Ag/CuFeS_2$ was −0.27 V (*vs.* NHE) [26]. As the conduction band of $CuFeS_2$ QDs was located at −0.11 V (*vs.* NHE) as shown in Fig. S1c (Supporting information), the conduction band of $Ag/CuFeS_2$ was much more negative than that of the $CuFeS_2$, which theoretically indicated that the $Ag/CuFeS_2$ material was characterized with an enormous reduction potential. Moreover, the surface carrier-migration efficiencies could be characterized *via* electrochemical impedance spectroscopy (EIS) [27]. As shown in Fig. 1f, the semicircle diameter of the EIS Nyquist plot of $Ag/CuFeS_2$ was smaller than that of $CuFeS_2$ QDs, suggesting that the introduced Ag single-atomic species could lower the interfacial charge-transfer resistance, which could facilitate the separation and migration of the carriers. The above results suggested that $Ag/CuFeS_2$ showed superior carriers separation ability and faster charge transfer efficiency.

The morphology together with the chemical composition in $Ag/CuFeS_2$ was detected by high-angle annular dark-field (HAADF) image and energy-dispersive X-ray spectroscopy (EDS) under scanning transmission electron microscopy mode (STEM). The HAADF-STEM image of $Ag/CuFeS_2$ in Fig. 2a indicated that the as-synthesized QDs were with a homogenous size distribution of an average diameter of *ca.* 6.8 nm. Individual Ag atoms in catalysts could be distinguished in the aberration-corrected HAADF-STEM images. As shown in Fig. 2b, Ag single atoms (marked with the white circles) were uniformly dispersed on the surfaces of $CuFeS_2$ QDs, which revealed that only Ag single atoms were present; there were no Ag nanoparticles formed. The enlarged HAADF-STEM im-

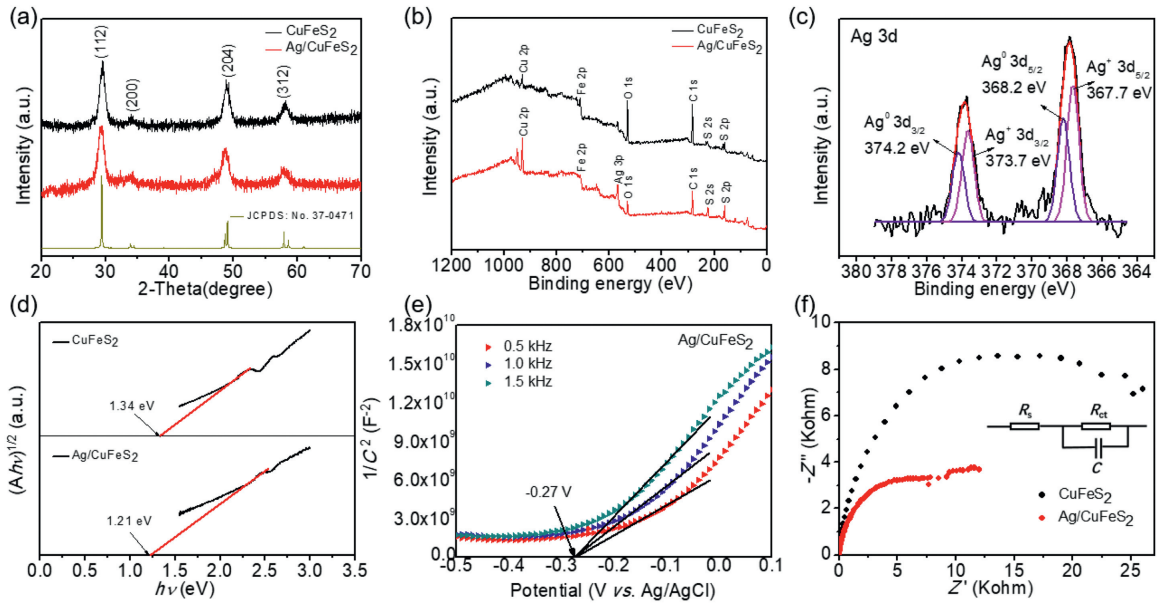

Fig. 1. Crystal structure and electronic structure characterization of $CuFeS_2$ and $Ag/CuFeS_2$ QDs. (a) XRD patterns. (b) XPS survey spectra. (c) High-resolution XPS spectra of Ag 3d (d) Bandgaps. (e) Mott-Schottky curves. (f) EIS Nyquist plots of QDs electrodes measured under the open-circuit potential with natural light irradiation.

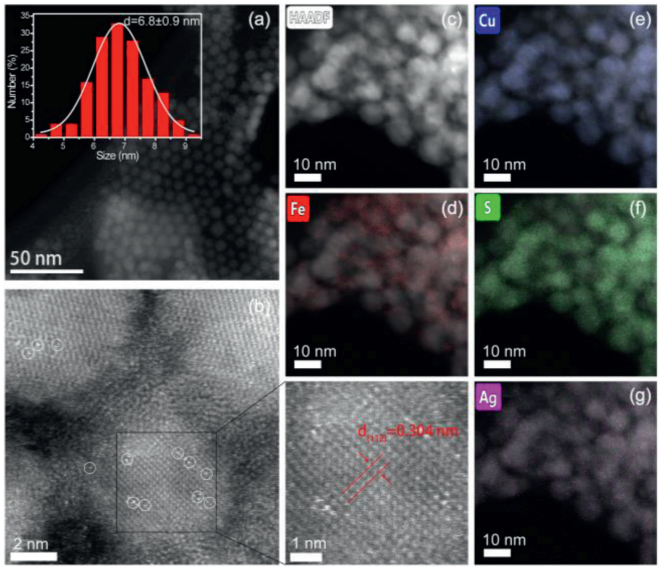

Fig. 2. Morphology characterizations of $Ag/CuFeS_2$. (a) HAADF-STEM image of $Ag/CuFeS_2$. (b) Aberration-corrected HAADF-STEM image (left) of Ag single atoms (white dots in the circles) on $CuFeS_2$ QD support and magnified HAADF-STEM image (right) of the square marked with red dots. STEM-EDS mapping of element distribution within (c) $Ag/CuFeS_2$; (d) Fe; (e) Cu; (f) S; (g) Ag.

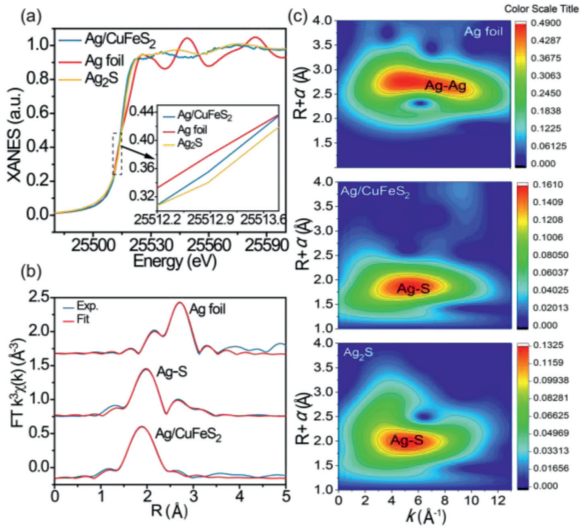

Fig. 3. X-ray absorption spectroscopy characterization of $Ag/CuFeS_2$. (a) Ag K-edge XANES spectra of Ag foil, Ag_2S and $Ag/CuFeS_2$. (b) Fourier transform of k^3-weighted Ag K-edge EXAFS fitting curve in R-space. (c) Wavelet transforms analysis of Ag foil, Ag_2S and $Ag/CuFeS_2$.

age (right) in Fig. 2b showed that the $Ag/CuFeS_2$ had a lattice spacing of 0.304 nm, which corresponding to the *d*−spacing of the crystallographic (112) plane of tetragonal phase $CuFeS_2$ QDs. The elemental compositions of Fe, Cu, S, and Ag were homogeneously distributed within the catalyst as verified by the STEM-EDS mapping images in Figs. 2c-g.

It was of great interest to further probe the accurate local structure of Ag single atoms on $CuFeS_2$ QDs. Thus the highly-sensitive electronic and local coordinational structure probing techniques, such as the extended X-ray absorption fine structure (EXAFS) and X-ray absorption near-edge structure (XANES) spectroscopy were further used to confirm the valence state and local coordinational environment for Ag [28]. As shown in Fig. 3a, the Ag K-edge XANES of $Ag/CuFeS_2$ was located between Ag foil and Ag_2S, which double confirmed the mixed-valence Ag(I) and Ag(0) in $Ag/CuFeS_2$ and was consistent with the XPS observation. Moreover, Fig. 3b showed the Fourier transforms (FTs) of the k^3-weighted EXAFS oscillations of the as-prepared $Ag/CuFeS_2$, together with the standard references of Ag_2S and Ag foil. According to the EXAFS fitting results, no Ag–Ag coordination peak at 2.87 Å was observed, demonstrating that Ag in $Ag/CuFeS_2$ did exist in the isolated single-atomic state, and there was no Ag nanoparticle formed. Moreover, the atomic distance of Ag–S in $Ag/CuFeS_2$ was ~2.48 Å, which was similar to the Ag–S bond distance of ~2.51 Å in Ag_2S, indicating that part of the single-atomic Ag(I) was coordinated with S in $Ag/CuFeS_2$ (Table S2 in Supporting information). Furthermore, an intensity maximum at 5.8 $Å^{-1}$ can be observed from the wavelet transform (WT) contour plots of $Ag/CuFeS_2$ (Fig. 3c), which can be assigned to

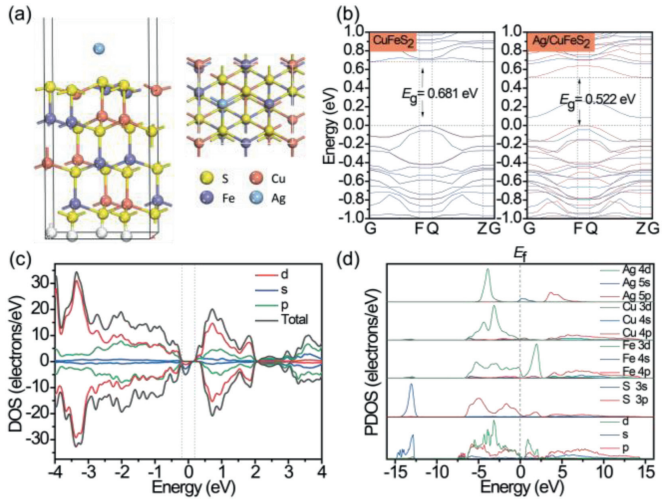

Fig. 4. DFT calculations of band structure and density of state. (a) Adsorption sites (left) of Ag on $CuFeS_2$ (112) surface and top view (right) of $Ag/CuFeS_2$ (112) surface. (b) Band structure of tetragonal phase $CuFeS_2$ and $Ag/CuFeS_2$. (c) DOS of $Ag/CuFeS_2$. (d) PDOS of $Ag/CuFeS_2$.

Ag–S coordination without an Ag–Ag signal. Therefore, it can be concluded that the single atomic $Ag/CuFeS_2$ QDs were successfully synthesized.

To further understand the electronic structure of $Ag/CuFeS_2$, DFT calculations were employed. We have considered three different adsorption sites (Fe, Cu, S) for Ag to investigate the effects of single Ag adsorption on the $CuFeS_2$ (112) surface structures, as shown in Fig. 4a. The adsorption energies of single Ag atom adsorption on the $CuFeS_2$ (112) plane of the three sites were negative (Table S3 in Supporting information), indicating that the whole process was spontaneous exothermic transformation [29]. Besides, we have found the lowest adsorption energy was at the S center site; thus, we hypothesized that Ag was most likely to bind with S atoms to form Ag–S [30,31]. As shown in Fig. 4b, the calculated band structure showed that $Ag/CuFeS_2$ was an indirect bandgap semiconductor with a bandgap of 0.522 eV, which was narrower than the 0.681 eV bandgap of $CuFeS_2$ QDs. Due to the introduction of Ag single atoms, the conduction band minimum (CBM) edge moved to lower energy, which could contribute to a narrowing overall energy gap in $Ag/CuFeS_2$ [32]. This tendency was consistent with the observed results from the Mott-Schottky curve and ultraviolet-visible (UV–vis) spectra. Moreover, an obvious impurity energy level between valence band maximum (VBM) and CBM in $Ag/CuFeS_2$ could be observed, which was beneficial for the electron transition from the valence band (E_{VB}) to the conduction band (E_{CB}) and further promoted the separation of photogenerated electron-hole pairs. As shown in Figs. 4c and d, the orbital interaction between Ag atoms and $Ag/CuFeS_2$ (112) plane was further investigated by the density of states (DOS) and the partial density of states (PDOS). After the introduction of Ag atoms, S 3p orbital and a hybrid orbital of Ag 4d, Fe 3d, Cu 3d contributed to the VBM, while the density state at the CBM was mainly attributed to Fe 3d and S 3p orbitals. Moreover, compared with $CuFeS_2$ QDs (Fig. S2 in Supporting information), a hybrid state density appeared at the forbidden band. The PDOS showed that the hybrid density was formed *via* the hybridization of Ag 5s and Fe 3d orbitals. Hence, the theoretical calculation results suggested that the bandgap reduction could enhance the light absorption capacity in $Ag/CuFeS_2$, and the presence of impurity energy levels formed a new charge transfer channel to improve the efficiency of the carrier separation, which was expected for the improvement of the photocatalytic activity [27].

Considering the narrower bandgap feature within $Ag/CuFeS_2$, it would be interesting to employ this material for environmental pollutants removal. The optical response spectrum range as well as the carrier separation efficiency, are expected to be enhanced compared to the original $CuFeS_2$ QDs. Herein, RhB, which is a typical organic dye in dyeing wastewater [33], have been employed in the experiment. Prior to the degradation experiment, the initial pH value of the solution could influence the adsorption and degradation efficiency by affecting the surface complexation and the electrostatic interactions between the adsorbate and the QDs surface [34]. The degradation efficiencies of $Ag/CuFeS_2$ were investigated under a broad range of pH from 2, 4, 6, 8 to 10. Under each pH, the reaction time was set to be 60 min. It has been observed that the fastest degradation rate occurred when the initial RhB solution (5 mg/L) was at pH 6, as shown in Fig. S3a (Supporting information). RhB is a cationic dye; the faintly acidic is favourable for the disassociation of protons, which facilitating the adsorption and photocatalytic degradation of RhB. Based on these pre-experimental results, the degradation performance of the $Ag/CuFeS_2$ was investigated under the optimal reaction conditions. As shown in Fig. 5a, under the optimal pH condition, the degradation efficiency of $Ag/CuFeS_2$ reached as high as 90% within the first 10 min, which was 3.55 times higher than that of $CuFeS_2$ QDs. The decrease of concentration was evident by the reduction of the peak intensity at 554 nm in the UV–vis absorption spectra of RhB solution in the experiments (Figs. S3b and c in Supporting information). To understand the reaction kinetics, both the *pseudo*-first-order and *pseudo*-second-order kinetic models were applied to simulate the reaction process [35]. According to the fitting results, the *pseudo*-second-order kinetic model (Fig. 5b) was more suitable for describing the degradation process compared with the *pseudo*-first-order kinetic model (Fig. S3d in Supporting information) under different catalyst conditions. The fitting parameters indicated that $Ag/CuFeS_2$ had a faster degradation rate (Table S4 in Supporting information). This could be attributed to a variety of interactions in the adsorption process, including the electrostatic interaction as well as the hydrogen bonding [36]. To further identify the active species and explore the photocatalytic mechanism of the high activities in $Ag/CuFeS_2$ [37,38], a series of species quenchers, including isopropanol (IPA, 1 mmol/L), benzoquinone (BQ, 1 mmol/L), and bicarbonate ($NaHCO_3$, 1 mmol/L) were employed to scavenge the active species, such as hydroxyl radicals ($^{\bullet}OH$), superoxide radicals ($O_2^{\bullet-}$), and photon-generated holes (h^+). The degradation curve (Fig. 5c) indicated that h^+ was the main reactive species in the degradation process, and the addition of BQ to capture $O_2^{\bullet-}$ also slightly inhibited the degradation efficiency, while $^{\bullet}OH$ could be ignored. Considering the variation of the positions of the conduction band and valence band, a possible electron and hole transfer process could be further explored. As the conduction band of $Ag/CuFeS_2$ was more negative than the $E_0(O_2/O_2^{\bullet-}) = -0.046$ V; therefore, the electrons in the conduction band could react with the oxygen dissolved in water to form $O_2^{\bullet-}$. However, the potential of the $Ag/CuFeS_2$ valence band was more negative than that of the $E_0(^{\bullet}OH/H_2O) = +2.68$ V, so h^+ could not be oxidized to generate $^{\bullet}OH$ [39]. According to the structural mechanism of $Ag/CuFeS_2$, the active species in the photocatalytic system were mainly h^+ and $O_2^{\bullet-}$, which was consistent with the conclusion obtained from the free radical quenching experiments. Combining with the active species explored, the photocatalytic mechanism could be described by the following equations (Eqs. 1–4):

$$\text{Catalysts} + h\nu \rightarrow h^+ + e^- \quad (1)$$

$$\text{RhB} + h^+ \rightarrow CO_2 + H_2O \quad (2)$$

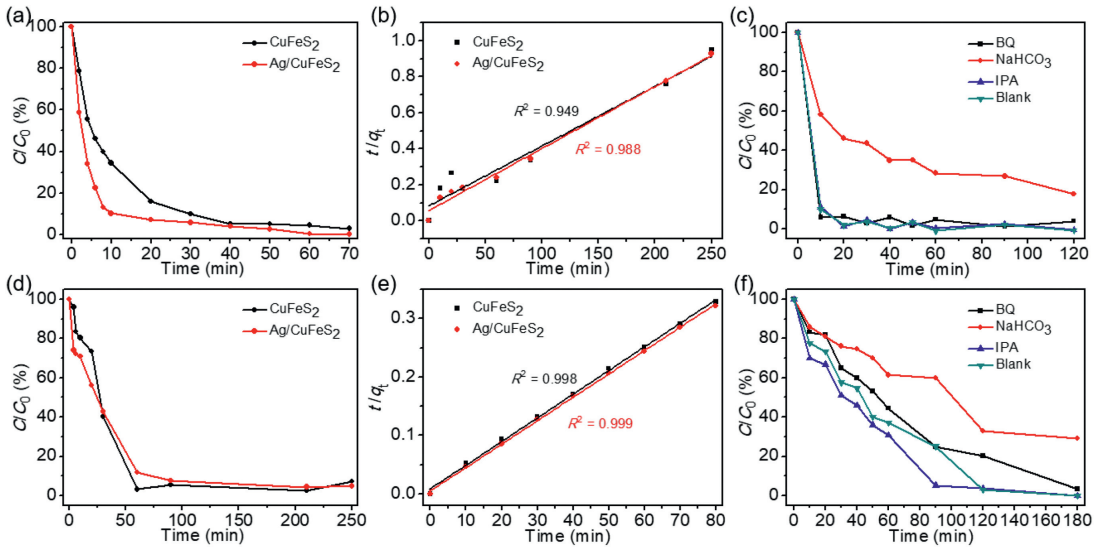

Fig. 5. Cr(VI) and RhB removal experimental data. (a) Photocatalytic degradation behaviours of RhB with different catalysts. (b) *Pseudo*-second-order fitting of RhB degradation. (c) The effects of different scavengers on the degradation of RhB over $Ag/CuFeS_2$. (d) Photocatalytic removal behaviours of Cr(VI) with different catalysts. (e) *Pseudo*-second-order fitting of Cr(VI) removal. (f) Effects of different scavengers on the degradation of Cr(VI) over $Ag/CuFeS_2$.

$$O_2 + e^- \rightarrow O_2^{\bullet -} \quad (3)$$

$$RhB + O_2^{\bullet -} \rightarrow CO_2 + H_2O \quad (4)$$

Besides organic dye, Cr(VI) salts are typical inorganic dyes that have also been frequently used in the leather industry [40]. They can easily enter into industry dyeing wastewater and causing heath problems severely. Benefited from the existence of the mixed redox-couple Cu(I)–S–Fe(III) inside the tetragonal phase $CuFeS_2$ crystal structure, together with the rise of the CBM resulting in a larger reduction potential in $Ag/CuFeS_2$ QDs, the efficiency and mechanism of $Ag/CuFeS_2$ QDs on Cr(VI) removal has been studied. As shown in Fig. S4a (in Supporting information), Cr(VI) reduction under various initial pH values (pH 2, 4, 6, 8, 10) were explored. The results showed that the highest photocatalytic reduction efficiency for Cr(VI) was at pH 2. The removal rate was 95.7% within 250 min, as shown in Fig. 5d. The fast reaction was benefited from the acidic conditions, as sufficient protons (H^+) could promote the transformation of Cr(VI) to Cr(III) of the $E_0(Cr(VI)/Cr(III)) = +1.33$ V [41]. The mechanism of the reduction of Cr(VI) by $Ag/CuFeS_2$ QDs could be explained by the following Eqs. 1, 5, 6:

$$Cr_2O_7^{2-} + 14H^+ + 6e^- \rightarrow 2Cr^{3+} + 7H_2 \quad (5)$$

$$CrO_4^{2-} + 4H_2O + 3e^- \rightarrow 2Cr(OH)_3 + 5OH^- \quad (6)$$

Moreover, comparing the performance of $CuFeS_2$ QDs with the $Ag/CuFeS_2$ QDs, the Cr(VI) removal efficiency of $Ag/CuFeS_2$ QDs in the first 10 min was approximately 6.75 times higher than that of the $CuFeS_2$ QDs. As the reaction progressed, the reaction rate was slower than that of the $CuFeS_2$. The possible explanation was that the reaction rate of $Ag/CuFeS_2$ was very high in the initial reaction period that led to the consumption of a large number of photoelectron (e^-) and thus resulted in the accumulation of h^+ in the valence band, so the process of the reaction was hindered [42]. Comparing the two fitting curves by the kinetic models, the *pseudo*-second-order kinetic model (Fig. 5e) was more suitable than the *pseudo*-first-order fitting model (Fig. S4b in Supporting information) for the description of the removal process under different catalytic conditions. The fitting parameters were listed in Table S5 (Supporting information). To evaluate the active species during the reaction process, the radical quenching experiments were conducted under the optimal conditions (Fig. 5f). Based on the consequence of the quenching experiments, e^- and $O_2^{\bullet -}$ were identified to be the main active species in Cr(VI) reduction [43], as molecular oxygen was found to consume part of the photogenerated electrons to produce $O_2^{\bullet -}$. Thus the elimination of $O_2^{\bullet -}$ significantly suppressed the photoreduction of Cr(VI), indicating that $O_2^{\bullet -}$ mediated indirect reduction should govern the photoreduction of Cr(VI) [44]. The addition of $NaHCO_3$ increased the pH, which inhibited the photocatalytic reaction efficiency, while the reaction rate was increased by adding IPA to capture $^{\bullet}OH$. Because $^{\bullet}OH$ had oxidation property, the as-formed Cr(III) during the reaction could be re-oxidized to Cr(VI), which was not conducive to the removal of Cr(VI); thus the reduction of $^{\bullet}OH$ by IPA increased the reaction rate. Moreover, the $^{\bullet}OH$ species may be generated by other pathways, because the potential of the $Ag/CuFeS_2$ valence band was found to be more negative than that of $E_0(^{\bullet}OH/H_2O) = +2.68$ V, so h^+ could not be oxidized to generate $^{\bullet}OH$. The experimental results were also consistent with the structural mechanism.

Combined with the above reaction mechanism study, we further employed $Ag/CuFeS_2$ QDs for the simultaneous Cr(VI) reduction and RhB degradation to reasonably use the photogenerated electron-hole pairs and maximization of the photocatalytic efficiency. As shown in Fig. S5a (Supporting information), the reduction efficiency of Cr(VI) and the degradation efficiency of RhB were significantly improved at neutral pH in the Cr(VI)/RhB mixture solution, in comparison with single pollutant systems at the same pH. In a single pollutant system that only contained RhB or Cr(VI), 95.2% of RhB and 30.2% of Cr(VI) were removed by $Ag/CuFeS_2$ after 2 h natural light radiation. However, in a mixture pollutants solution with both RhB and Cr(VI), the removal efficiencies for RhB and Cr(VI) in 2 h were as high as 97.3% and 79.4%, respectively, because the degradation of RhB could accelerate the separation of photogenerated electron-hole pairs to avoid the carriers aggregation and thus improve the reduction efficiency of Cr(VI). The quenching experimental results (Figs. S5b and c in Supporting information) indicated that $O_2^{\bullet -}$ and h^+ were the main active species in the catalytic process. Moreover, EPR spectra exhibited high-intensity signals of $O_2^{\bullet -}$, which was generated in the photocatalytic process (Eq. 3). The production of $O_2^{\bullet -}$ depended on e^-, and the number of e^- was closely related to h^+, thus the primary

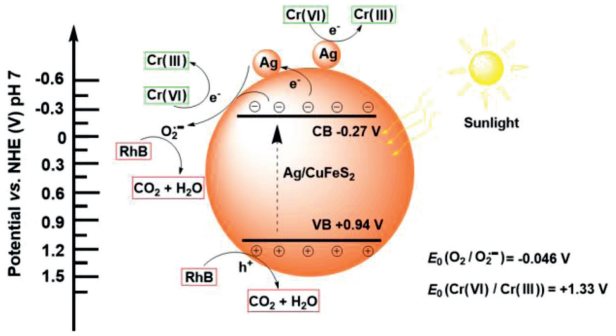

Fig. 6. Mechanism of simultaneous Cr(VI) reduction and RhB degradation over $Ag/CuFeS_2$.

function of h^+ was the degradation of RhB, whereas the consumption of h^+ accelerated part of the electrons to migrate to the surface to carry the Cr(VI) reduction and the other part would react with O_2 to form $O_2^{\bullet-}$ to facilitate RhB degradation. Based on the analysis mentioned above, it could be concluded that $Ag/CuFeS_2$ could synergistically promote the photocatalytic efficiency of the Cr(VI) reduction and RhB degradation.

Furthermore, we used river water and tap water to simulate the environmental-related industrial dyeing wastewater to test the catalytical performance of $Ag/CuFeS_2$ in real dyeing wastewater treatment applications. As shown in Fig. S6 (Supporting information), the efficiency of the Cr(VI) reduction and RhB degradation was similar to that in deionized water, which indicates that the complex contaminants such as dissolved organic matter, inorganic ions within tap water or natural river water would not significantly influence the photocatalytic performance of $Ag/CuFeS_2$. Moreover, Fig. S7 (Supporting information) showed a well consistent activity remain by employing $Ag/CuFeS_2$ for six consecutive catalytic cycles in Cr(VI)/RhB mixture solution. After six cycling catalytic tests, Cr(VI) removal efficiency was well preserved, which confirmed the excellent stability of $Ag/CuFeS_2$. Fig. S5d (Supporting information) presented the XRD patterns of $Ag/CuFeS_2$ before and after the pollutant removal reaction, where the prominent diffraction peaks of $Ag/CuFeS_2$ remained invariable. Moreover, XPS spectra of Ag (Fig. S8 in Supporting information) after the reaction demonstrated that the valence states of Ag atoms were still mixed-valence (Ag(0) and Ag(I)), which were steadily deposited on $CuFeS_2$, suggesting significant phase stability of $Ag/CuFeS_2$.

The mechanism of synergistic Cr(VI) reduction and RhB degradation over $Ag/CuFeS_2$ was illustrated in Fig. 6. At different reaction stages, the Ag atom acted as an effective electron shutter to accept or release electrons [45]. Under sunlight irradiation, the electrons could be excited quickly from VBM to CBM of the $CuFeS_2$ QDs. Subsequently, the electron transfer from the excited $CuFeS_2$ QDs into Ag created an interfacial charge equilibrium and electron accumulation on Ag, which was beneficial for the photocatalysis reaction with contaminants. Also, it was demonstrated by the DFT results that the formation of the impurity level contributed to carrier separation. The excited electrons could be transferred from the CBM of $CuFeS_2$ QDs to Ag(0), followed by the reaction with adsorbed on the surface of $Ag/CuFeS_2$ to produce $O_2^{\bullet-}$. The photogenerated holes left on the VBM of $CuFeS_2$ QDs could react directly with the pollutants. According to the above discussion against the experimental results as well as theoretical calculation, a possible photocatalytic mechanism of the enhanced photocatalytic activity was proposed based on the energy band structures of $Ag/CuFeS_2$ as follows: (1) With the reduction of the bandgap, the material could be excited by natural UV–vis-NIR light, which improved the efficiency of photon utilization; (2) the mixed-valence Ag(0) and Ag(I) single atoms formed in $Ag/CuFeS_2$ could effectively separate photon-generated carriers; (3) the metallic Ag(0) had excellent electrical conductivity, which could accelerate the movement of free-electron onto the semiconductor surface, which further enhanced the separation of photogenerated carriers, and thus more free electrons and holes could be obtained to react with the target contaminants; (4) the specific surface area of the spherical $CuFeS_2$ QDs was relatively large, which could absorb more targeted pollutants, accelerating the reaction between photocarriers and target molecules to improve the photocatalytic efficiency.

In this work, we developed a novel single-atomic $Ag/CuFeS_2$ semiconducting photocatalyst for dyeing wastewater treatment. The catalyst consists of the tetragonal phase $CuFeS_2$ QDs decorating with uniformly dispersed mixed-valence Ag single atoms. We discovered that the introduction of single-atomic Ag atoms could facilitate the engineering of the bandgap of $CuFeS_2$ QDs, which is conducive for synergistically reduce the Cr(VI) and oxidize RhB in dyeing wastewater. Combined with the experimental results as well as DFT calculations, the formation and catalytic mechanisms of monatomic catalysts were illustrated. The narrow bandgap of $Ag/CuFeS_2$ (1.21 eV) promotes the extension of the absorption spectrum from UV–vis to NIR. Meanwhile, the as-formed mixed-valence Ag(0) and Ag(I) single atoms in $Ag/CuFeS_2$ can effectively separate photon-generated carriers, thus enhancing the photocatalytic activity toward the degradation of organic dye or the reduction of inorganic dye. These findings provide new insights into the design of single-atomic catalysts for dye removal in dyeing wastewater.

Declaration of competing interest

The authors report no declaration of competing interests.

Acknowledgements

This work was financially supported by the National Natural Science Foundation of China (Nos. 21777045, 61875119), Distinguished Young Scholar Fund from Natural Science Funds of Guangdong Province, China (No. 2020B151502094), the program for Professor of Special Appointment (Eastern Scholar) at Shanghai Institutions of Higher Learning, Shanghai Rising-Star Program (No. 19QA1404000), and Shanghai Talent Development Fund. We would like to thank Ceshigo research service "www.ceshigo.com" for his contribution to the X-ray absorption spectroscopy (XAS) measurements. We are grateful to the analysis center at the school of environmental science, engineering, and SUSTech Core Research Facilities (SCRF) at the southern university of science and technology. We express our special thanks to Prof. Le-Le Duan for the help on the UV–vis absorption spectra measurement.

Supplementary materials

Supplementary data associated with this article can be found, in the online version, at doi:10.1016/j.cclet.2021.05.040.

References

[1] M. Ahmad, M. Yousaf, A. Nasir, et al., N. Mahmood. Environ, Sci. Technol. 53 (2019) 2161–2170.
[2] S. An, G. Zhang, T. Wang, et al., ACS Nano 12 (2018) 9441–9450.
[3] Y. Chen, J. Gao, Z. Huang, et al., Environ. Sci. Technol. 51 (2017) 7084–7090.
[4] Q. Ge, X. Feng, R. Wang, et al., Environ. Sci. Technol. 54 (2020) 8022–8031.
[5] N. Wu, X. Liu, M. Zeng, et al., J. Nanoparticle Res. 21 (2019) 268–278.
[6] T. Yan, Y. Li, X. Song, J. Wang, Z. Xie, D. Deng, J. Mater. Chem. C 7 (2019) 7279–7287.
[7] W. Girma, S. Tzing, P. Tseng, et al., ACS Appl. Mater. Interfaces 10 (2018) 4590–4602.
[8] J. Zou, Y. Chen, S. Liu, et al., J. Crittenden, Water Res. 150 (2019) 330–339.
[9] U. Rajaji, K. Murugan, S. Chen, et al., Compos. Part B: Eng. 160 (2019) 268–276.
[10] J. da Silveira Salla, K. da Boit Martinello, G.L. Dotto, et al., Colloids Surfaces A: Physicochem. Eng. Asp. 595 (2020) 124679–124687.

[11] J. Qi, H. Lan, R. Liu, H. Liu, J. Qu, Water Res. 171 (2020) 115448.
[12] C. Zhou, Y. Zhou, B.E. Rittmann, Water Res. 119 (2017) 91–101.
[13] J. Park, S. An, E.H. Jho, et al., Water Res. 185 (2020) 116242.
[14] J. Gao, H. Yang, X. Huang, et al., Chem 6 (2020) 658–674.
[15] Y. Wang, X. Shang, J. Shen, et al., Nat. Commun. 11 (2020) 3043.
[16] S. Woo, S. Choi, S. Kim, et al., ACS Catal 9 (2019) 2580–2593.
[17] S. Ma, S. Zhan, Y. Jia, Q. Shi, Q. Zhou, Appl. Catal. B: Environ. 186 (2016) 77–87.
[18] X. Fang, Q. Shang, Y. Wang, et al., Adv. Mater. 30 (2018) 1–7.
[19] S.K. Sahoo, Y. Ye, S. Lee, et al., ACS Energy Lett. 4 (2019) 126–132.
[20] G. Li, Z. Lian, W. Wang, D. Zhang, H. Li, Nano Energy 19 (2016) 446–454.
[21] T.E. Engin, A.V. Powell, S. Hull, J. Solid State Chem. 184 (2011) 2272–2277.
[22] M. Zhu, P. Chen, M. Liu, ACS Nano. 5 (2011) 4529–4536.
[23] X. Xiao, L. Ge, C. Han, et al., Appl. Catal. B: Environ. 163 (2015) 564–572.
[24] A. Ghahremaninezhad, D.G. Dixon, E. Asselin, Electrochim. Acta 87 (2013) 97–112.
[25] X. Lv, J. Xu, G. Jiang, J. Tang, X. Xu, J. Colloid Interface Sci. 369 (2012) 460–469.
[26] A. Ishikawa, T. Takata, J.N. Kondo, et al., J. Am. Chem. Soc. 124 (2002) 13547–13553.
[27] J. Yan, J. Liu, Y. Ji, et al., ACS Catal. 10 (2020) 8742–8750.
[28] R. Shen, W. Chen, Q. Peng, et al., Chem 5 (2019) 2099–2110.
[29] W. Liu, Y. Li, F. Liu, et al., Water Res 151 (2019) 8–19.
[30] T. Liu, B. Liu, L. Yang, et al., Appl. Catal. B: Environ. 204 (2017) 593–601.
[31] Y. Chen, Z. Huang, M. Zhou, et al., Environ. Sci. Technol. 51 (2017) 2304–2311.
[32] X. Xiao, Y. Gao, L. Zhang, et al., Adv. Mater. 32 (2020) 2003082.
[33] H. Xu, M. Prasad, X. He, L. Shan, S. Qi, Sci. China, Ser. E Technol. Sci. 52 (2009) 3054–3060.
[34] L. Wang, M. Cao, Z. Ai, L. Environ. Sci. Technol. 49 (2015) 3032–3039.
[35] R. Chattot, T. Asset, P. Bordet, et al., ACS Catal. 7 (2017) 398–408.
[36] I. Park, D.O. Atienza, A.M. Hofstead-Duffy, D. Chen, Y.J. Tong, ACS Catal. 2 (2012) 168–174.
[37] Y. Yu, C. Cao, H. Liu, et al., J. Mater. Chem. 2 (2014) 1677–1681.
[38] G.V. Buxton, C.L. Greenstock, W.P. Helman, A.B. Ross, J. Phys. Chem. Ref. Data. 17 (1988) 513–886.
[39] Y. Yin, L. Shi, W. Li, et al., Environ. Sci. Technol. 53 (2019) 11391–11400.
[40] J. Ding, Y. Pan, L. Li, et al., Chem. Eng. J. 384 (2020) 123232.
[41] X. Yi, S. Ma, X. Du, et al., Chem. Eng. J. 375 (2019) 121944.
[42] Q. Xu, L. Zhang, B. Cheng, J. Fan, J. Yu, Chem 6 (2020) 1543–1559.
[43] D. Xia, W. Xu, Y. Wang, et al., Environ. Sci. Technol. 52 (2018) 13399–13409.
[44] G. Dong, L. Zhang, J. Phys. Chem. C 117 (2013) 4062–4068.
[45] L. Zhang, D.A. Blom, H. Wang, Chem. Mater. 23 (2011) 4587–4598.